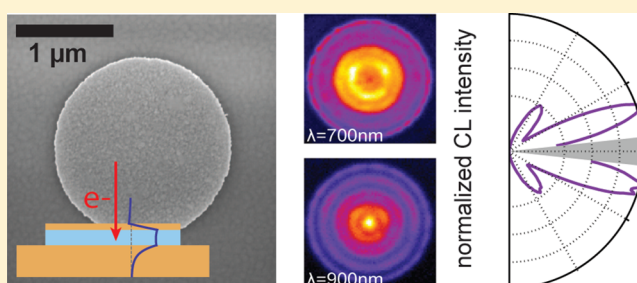# Nanoscale Excitation Mapping of Plasmonic Patch Antennas

Abbas Mohtashami, Toon Coenen, Alessandro Antoncecchi, Albert Polman, and A. Femius Koenderink*

Center for Nanophotonics, FOM Institute AMOLF, Science Park 104, 1098 XG Amsterdam, The Netherlands

ABSTRACT: We experimentally investigate the resonant modes of plasmonic patch antennas using angle-resolved cathodoluminescence imaging spectroscopy. Plasmonic modes residing in the patch antenna are locally excited using a scanning electron beam, providing high-resolution spectral and spatial maps of the modes of patch antennas corresponding to variations in the local density of optical states in the antennas. A semianalytical model is used to qualitatively explain the experimentally observed modes. Furthermore, emission patterns, directionality, and beam steering properties of patch antennas are studied in different patch sizes and at different wavelengths. Strong directionality and control over the output beam angle as a function of excitation position are observed. A distributed dipole model is used to explain the radiation pattern and beam width of the patch antenna radiation, which shows a good agreement with experiment.

KEYWORDS: plasmonics, nanoscale optical cavity, surface plasmon polaritons, cathodoluminescence, optical antenna, directional emission, Purcell effect

For technological applications in improving light sources, LEDs, and fluorescence microscopy, as well as for breakthroughs in quantum optics, many efforts are devoted to optimizing light extraction from single emitters.[1,2] Among strategies to realize ultrabright sources, researchers have pursued integration of active materials with dielectric structures that include microcavities,[3] Bragg stacks, photonic crystals,[4,5] and integration of sources with metallic nano-objects.[6] In particular, the field of "plasmonics" promises to enhance the brightness and directivity of light sources through a set of effects. First, at Ag, Au, and Al surfaces and particles, plasmon resonances feature strongly confined fields with very high per-photon field strength. On this basis one expects large local density of optical states (LDOS) enhancements that accelerate spontaneous emission decay of emitters into plasmon modes. Such acceleration of excited-state decay promises very high fluorescent photon flux per emitter when emitters are pumped near saturation. As a second effect, plasmonics can aid outcoupling of light into advantageous directions. The most established methodology is to generate "phased array antennas" such as Yagi–Uda plasmon antennas,[6–10] bull's eyes,[11,12] and plasmonic lattice antennas,[13,14] in which plasmon scatterers driven by the fluorophore act as secondary coherent sources so that a directional emission pattern can be obtained. A second, more recently proposed method is to use comparatively large scatterers in which a coherent superposition of multipoles can be excited that jointly show directional emission.[15,16] Finally, a third approach that was proposed in the pursuit of ultrabright single-photon sources is the use of so-called "patch antennas".[17,18] Such patch antennas rely on patches of metal several wavelengths across in which a nearby emitter can excite planar guided modes that scatter out at the edges.[19]

A particularly promising patch antenna that was recently introduced in refs 17 and 18 is based on circular patches with a metal–insulator–metal (MIM) geometry. In the radio frequency domain patch antennas are commonly used, as they have a very low profile and can be simply mounted on a flat surface over a ground plane.[20] When operating at a frequency that corresponds to the lowest order resonance where the antenna size matches half the wavelength, as is common for RF frequencies, one obtains a modest gain in directivity. In the optical domain, the proposition has been to operate at higher order resonance conditions, where multiple wavelengths fit in the patch diameter, which allows much higher directivity. Moreover, proper tuning of the metal–insulator–metal geometrical parameters ensures large Purcell factor designs. Belacel et al.[18] experimentally realized such patch antennas by making a thin dielectric film loaded with quantum dots on a thick gold surface. After pinpointing single quantum dots in the film, they could position circular gold patches of micrometers across centered on top of a single quantum dot and study the fluorescence decay rate before and after deposition of the patch. This type of geometry is expected to show a large LDOS enhancement due to the fact that the MIM geometry supports a guided plasmon mode that is tightly confined, with a very strong field in the gap, normal to the metal surfaces. Indeed, measured Purcell factors up to 80 have been reported.[18] Furthermore, theoretical analysis indicates that such MIM patch antennas give directional emission in a narrow "doughnut beam" normal to the patch, with an angular width of around 35° and a null at 0°, at least for embedded sources
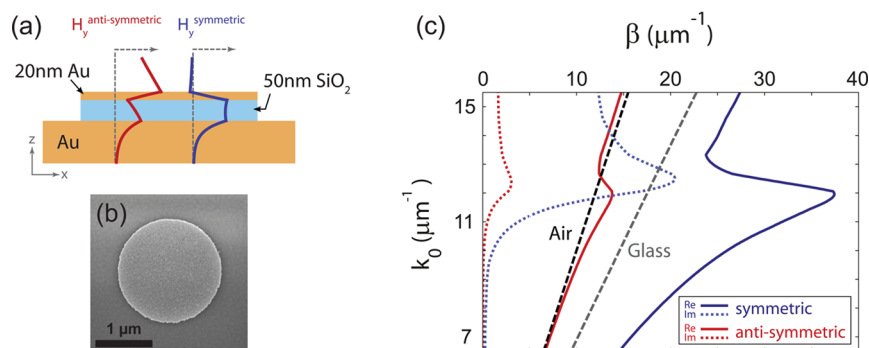
Figure 1. (a) Schematic of a patch antenna. The planarized MIM structure supports two transverse magnetic modes (H_y) with opposite symmetries. (b) SEM image of a fabricated patch antenna with a diameter of 1.8 μm. (c) Real (solid curves) and imaginary (dotted curves) parts of the dispersion relation of the planarized MIM structure of part (a) with two supported transverse magnetic modes. On the axes, k_0 and β represent free-space and MIM wavenumbers, respectively. Glass dispersion relation and light lines are also indicated for comparison.

oriented along the axis of maximum Purcell factor, i.e., normal to the patch. Observations rather point to narrow beams without a central null, which has been attributed to the directivity imparted on differently aligned and oriented sources. Directional emission is expected to come about because the tightly confined guided MIM mode excited by the emitter propagates to the disk edge, where it couples out as radiation into the far field. Since the entire patch edge is a coherent radiator, emission is expected to be directed, as fluorescence back-aperture imaging indeed shows according to ref 18.

The physics of patch antennas is expected to contain a set of salient features that are difficult to completely unravel in fluorescence experiments such as in single-emitter experiments, owing to the fact that one ideally would scan the point of excitation and the emission wavelength continuously while examining enhancements of the total emitted power, as well as directivity for different disk sizes. In this paper we perform exactly such a study using angle-resolved cathodoluminescence imaging spectroscopy (ARCIS).[21,22] To highlight the expected complexity of this system, calculations of the Purcell factor indicate that one expects a very large set of resonant modes with different radial and azimuthal quantum numbers that are simultaneously involved.[17,23,24] Cathodoluminescence imaging not only can be used to reveal such a complicated dependence of the local density of states on both frequency and excitation position but also allows one to answer the question of how such complex multimode systems can give robust directionality. This paper is structured as follows. First we present a simple analytical model for the mode structure and LDOS of circular MIM patch antennas. Subsequently we present measured spatial cathodoluminescence (CL) maps. Spatial maps indeed show a marked spatial and spectral structure in local density of states. Finally, we turn to the angular characteristics of differently sized patch antennas at various wavelengths and excitation positions. Commensurate with semianalytical modeling results, we find that patch antennas are more directional as they grow in size and that they show controllable beam steering as the excitation position is swept from the disk center to approximately half their radius.

THEORETICAL ANALYSIS AND CALCULATION

Figure 1a,b shows a sketch and scanning electron microscope (SEM) image of the sample geometry studied in this work, which is a MIM patch antenna geometry consisting of an extended gold substrate on top of which we fabricated circular patches that combine a 50 nm silica spacer and a 20 nm gold

layer. In this section we set up a simple analytical model for the expected mode structure and spatially dependent Purcell factor. Resonant modes of the patch antennas are analytically investigated using a Bessel-type standing-wave resonator model introduced by Filter et al.[23] They considered circular resonators that support propagating surface plasmon polaritons (SPPs) confined within the disk area. Here we apply this model to describe vertically stratified patch antennas that have a MIM geometry.

The MIM geometry of the patch antennas supports two transverse-magnetic (TM) plasmonic modes with opposite symmetries. Figure 1c shows a numerical calculation of the real (solid curves) and imaginary (dotted curves) part of the dispersion relation of the two modes for an infinitely extended MIM structure with the same layer thicknesses as our patches. As input for this calculation we use tabulated optical data,[25] inserted in a standard stratified system solver that solves for a complex wave vector at real frequency.[26] Symmetric (blue curve) and antisymmetric (red curve) modes are defined according to the symmetry of the magnetic field profile inside the structure as shown in Figure 1a. For comparison, the dispersion relation of the gap material, i.e., silica (gray dotted line), and the light line (black dotted line) of the surrounding air are also presented in the dispersion diagram. The antisymmetric mode has a dispersion relation very close to the light line, indicating a mode index close to air. However, the symmetric mode has a dispersion well beyond the light line, which indicates that the mode is strongly confined to the metal. This strongly dispersive and strongly confined MIM mode has been well studied in scattering experiments by Miyazaki et al.,[27,28] its dispersion has been studied in cathodoluminescence,[29] and this mode has been identified as responsible for large Purcell enhancements[18,30] for dipoles placed in the gap and oriented normal to the interfaces. On the basis of this high Purcell factor for polarizations matching the incident electron beam in our experiment, we expect to mainly excite the symmetric MIM mode in our CL experiment. Since the antisymmetric mode is weakly confined and almost index-matched with air, we expect that it does not contribute strongly to the scattered field at the abrupt edges of the antenna. Therefore, in the following we restrict our analysis to the symmetric mode contribution, which is also the mode identified as relevant in spontaneous emission experiments on the basis of Purcell factor calculations.[18]

In order to estimate the total collected CL intensity, we set up a simple semianalytical model for the local density of states
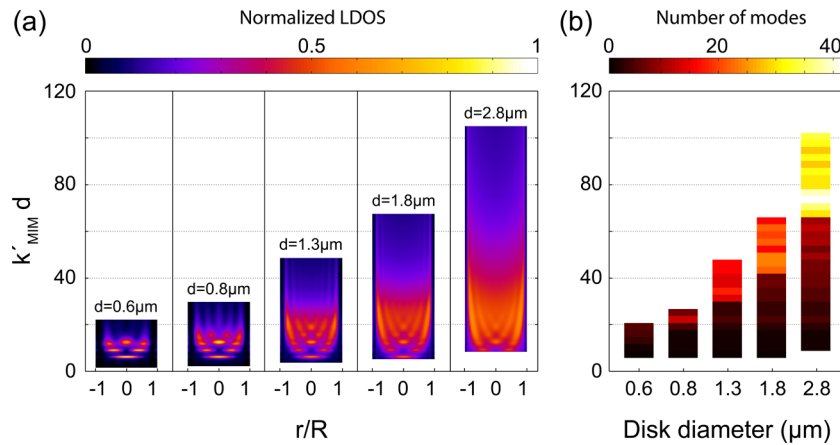
Figure 2. (a) Calculated spatial LDOS maps for five different disk sizes as a function of normalized wavenumber $k_{MIM}'d$ and distance to the center of the disk. (b) Histogram of the number of modes participating in the calculation of (a).

in the patch antenna starting from the model of Filter et al.,[23] which proceeds as follows. First we find the eigenfrequencies and mode profiles of eigenmodes. This step requires as ansatz for each mode profile that it factorizes as

$$E_z^m(r, z) = a(z)J_m(k_{MIM}r)e^{im\phi}$$

where $a(z)$ is the MIM waveguide mode profile, m is the azimuthal quantum number, J_m is a Bessel function, and k_{MIM} is the complex wave vector of the MIM mode at frequency ω. We note that in this ansatz, one assumes that the infinite-system symmetric MIM mode dominates. This means not only that the infinite-system asymmetric MIM mode is neglected but also that any contribution of modes that are bound to the patch edge and have in-plane wavenumber different from k_{MIM} are neglected. We expect this ansatz to be best for excitation positions away from the patch edge and for sufficiently large patches. According to García de Abajo and Kociak,[31] an impinging electron beam excites a structure not according to its LDOS at some height z but rather according to a projected LDOS obtained by integrating along the electron beam trajectory. We note that *within* our ansatz the z dependence and in-plane dependence factorize, meaning that integrating over z will not result in different information unless one goes beyond our ansatz.

From our ansatz, a discrete set of eigenmodes is obtained by imposing a reflective boundary condition at the MIM edge, which we write down so as to include a possible phase jump ϕ upon reflection (see Methods). In a second step, we estimate the LDOS from an expansion in terms of eigenmodes. The local density of states for a z-oriented dipole at position r is proportional to

$$N(\omega, r) \propto \sum_{n,m} |E_z^{n,m}(r)|^2 \mathcal{L}(\omega; \omega_{n,m}, \gamma) \tag{1}$$

Here the Lorentzian $\mathcal{L}(\omega; \omega_{n,m}, \gamma)$ replaces the traditional δ-function $\delta(\omega^2 - \omega_{n,m}^2)$ to account for the fact that the patch antenna modes have a large frequency width due to ohmic and radiative damping. For our calculations, the only two adjustable parameters of this model, i.e., the phase shift ϕ and damping γ, are extracted by matching to a COMSOL simulation (see below and Methods section for further details).

Figure 2a shows the calculated spatial LDOS maps of patch antennas for five different disk sizes. It should be noted that while each eigenmode has an azimuthal dependence ($e^{im\varphi}$

dependence), the LDOS does not. The wavelength on the vertical axis is converted to dimensionless wavenumber $k_{MIM}'(\lambda_0)d$ in order to facilitate direct comparison between different disk sizes, where k_{MIM}' is the real part of the MIM wave vector as reported in Figure 1c. For each disk, the physical frequency range that we report on corresponds to wavelengths from 525 to 4000 nm. For each disk size, the LDOS shows resonances, and the resonant bands show clear radial oscillations. In the RF domain one commonly uses the lowest order resonance, i.e., a $\lambda/2$ resonance spanning the disk diameter.[20] The highly directional operation proposed by Belacel[18] occurs at the resonant bands in which many modes participate. It would be tempting to explain the radial oscillations at higher size-to-wavelength ratios simply as a sequence of modes with monotonically increasing radial quantum number. However, the reader should be warned that radial and angular quantum numbers coexist, meaning that at higher frequencies the LDOS is composed of many modes, including those with high radial quantum number n and low azimuthal quantum number m, and vice versa. For reference, Figure 2b shows a histogram of the number of modes at different normalized wavenumbers and disk sizes corresponding to calculation of the modes in Figure 2a. The number of modes contributing to the LDOS within frequency bands of width γ is typically on the order of 10. The oscillations in LDOS vanish for higher wavenumbers due to larger ohmic damping at shorter wavelengths. Since the eigenfrequencies are only dependent on the fundamental quantity $k_{MIM}'(\lambda_0)d$ (i.e., the ratio between two length scales, the MIM wavelength and the disk size), one expects eigenmodes of differently sized disk antennas to occur at the same normalized wavenumber. However, this scaling is not perfect due to dispersion in the imaginary part of the MIM wave vector. The radial oscillation of the modes smear out for larger disk sizes due to the fact that larger disks support many modes that overlap and therefore cancel out the oscillations. Indeed for a very large disc, one would expect the LDOS to converge to that of a semi-infinite MIM film, which would be featureless except for Friedel oscillations[32] right at the film edge.

As further verification of this analytical model, we have also calculated the LDOS for patch antennas of 0.6 and 0.8 μm diameter using full-wave finite element simulations (see Methods for implementation in COMSOL). Figure 3 plots the result for the radiated power as a function of normalized
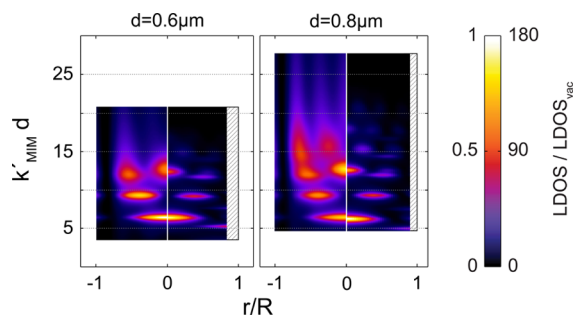
Figure 3. COMSOL-simulated radiation power for two disk diameters of 0.6 and 0.8 μm as a function of normalized wavenumber and distance to the center of the disk. For each disk size, the right part shows the COMSOL simulation radiated power, while the left part shows the corresponding calculated LDOS map of Figure 2a.

wavenumber and as a function of dipole position. For each disk size, the left part of the plot shows the calculated LDOS map corresponding to Figure 2a, and the right part shows the COMSOL-simulated maps. We have adjusted the phase and the resonance width in our calculation according to the COMSOL simulation for a range of k'_{MIM} values between 5 to 10 corresponding to the fundamental mode. We find good agreement between the analytical model and the full-wave simulation. Indeed, the COMSOL simulation likewise predicts a set of resonances, of which the lowest is localized at the disk center, while for higher frequencies resonances have an increasing set of antinodes across the disk perimeter and become increasingly close in frequency.

■ SPATIAL CATHODOLUMINESCENCE MAPS

In this section, we first present the results of the experimental CL measurements on patch antennas with different diameters, and then we compare them to the calculated LDOS maps. This comparison is motivated by the recently developed notion that the rate of excitation of the optical modes in plasmon structures by CL is approximately proportional to the LDOS,[22,33] so that the radiated CL intensity is expected to be proportional to the radiative part of the local density of optical states in the antenna. Figure 4 shows spatial maps of CL intensity for a
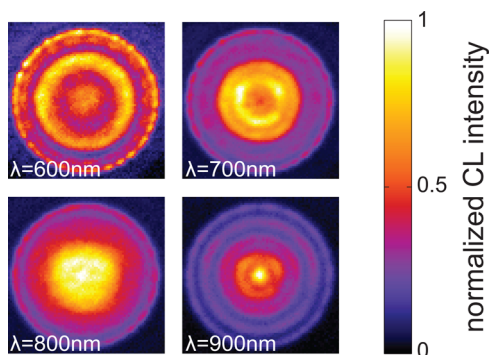

Figure 4. Spatial CL intensity maps of a typical patch antenna with disk diameter of 1.8 μm at four different wavelengths integrated over a bandwidth of 10 nm. CL intensity data are corrected for the background (typically around 100 cts/px/0.25 s) and the system response and are normalized to unity at each wavelength. The maximum counts of the raw map data before correction are equal to 320, 590, 370, and 350 cts/px/0.25 s for wavelengths from 600 to 900 nm, respectively.

typical patch antenna with disk diameter of 1.8 μm at four different wavelengths integrated over a bandwidth of 10 nm. Here, each pixel corresponds to a position of the electron beam at which the CL intensity is plotted. Due to the high spatial resolution of the scanning electron beam, a very detailed spatial map of the collected CL intensity can be obtained. The spatial intensity maps exhibit concentric rings within the disk area, reflecting the circular symmetry of the antenna. It should be noted that, since CL is an excitation spectroscopy technique, the profiles do not correspond to maps of (superpositions) of modes, but rather reflect the total power radiated out of the system due to the different superposition of modes excited for each excitation position on the patch antenna. In order to visualize the measured LDOS of the antennas more clearly, spatial CL intensity maps are azimuthally averaged at each wavelength (10 nm bandwidth), exploiting the radial symmetry of the patch antennas. Figure 5a shows azimuthally averaged
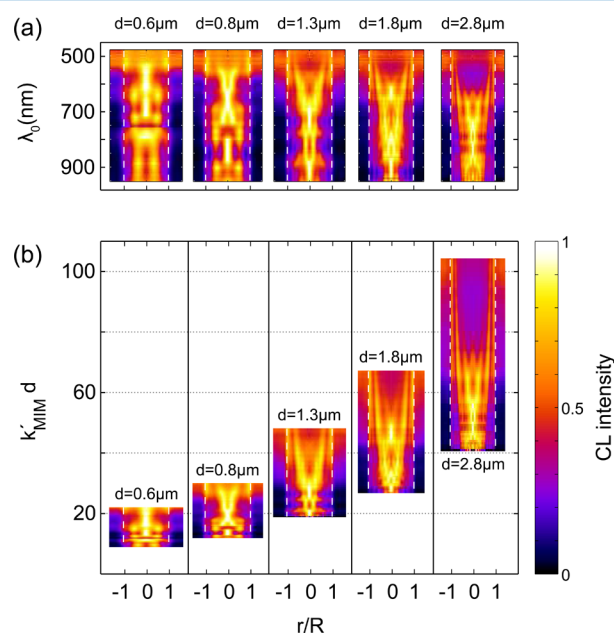

Figure 5. (a) Azimuthally averaged CL intensity maps as a function of wavelength and relative distance to the disk center for five disk sizes: 0.6, 0.8, 1.3, 1.8, and 2.8 μm. (b) CL intensity maps with normalized wavenumber for different disk diameters corresponding to (a). CL intensity data are corrected for the background (typically around 100 cts/px/0.25 s) and the system response and are normalized to unity at each disk size. The maximum counts of the raw map data before correction are equal to 1390, 1030, 990, 630, and 960 cts/px/0.25 s for increasing disk size, respectively.

CL intensity maps of five different patch antennas as a function of wavelength and distance to the center of the antenna. In order to directly compare the CL intensity maps of different disk sizes, wavelength values (λ_0) in Figure 5a are converted to dimensionless quantity $k'_{MIM}d$ using the calculated dispersion relation of the infinite MIM structure $k_{MIM'}(\lambda_0)$ (Figure 1c) and the disk diameter d.

In order to examine the relation between the CL intensity and LDOS, we compare the CL maps of Figure 5 to the LDOS maps of Figure 2 that were calculated with the simple model of Filter et al.[23] Experiment and calculation show qualitative similarities. These include the alternating occurrence of one, two, and three antinodes in radial LDOS dependence as one sweeps frequency, smearing of the radial oscillations at higher
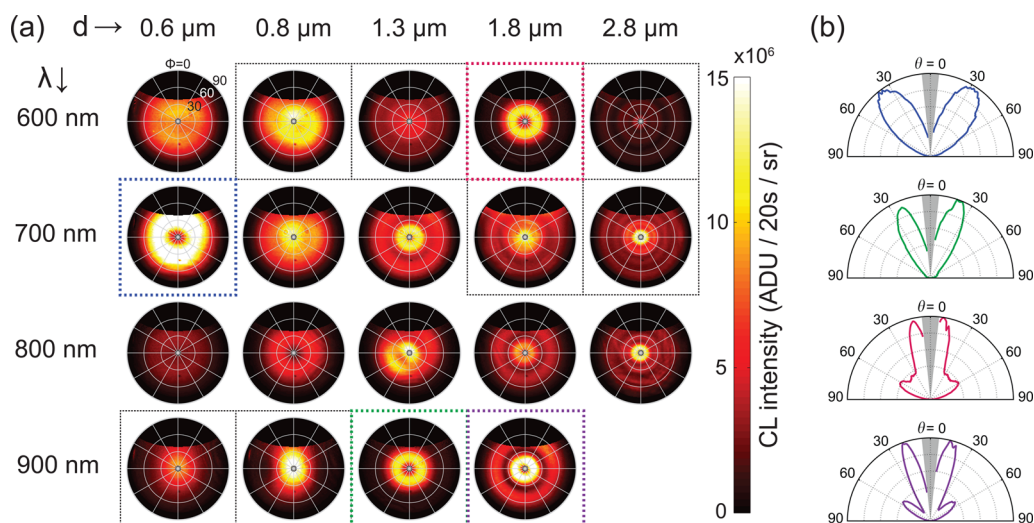
Figure 6. (a) Radiation patterns measured for different disk diameters (from left to right 0.6, 0.8, 1.3, 1.8, 2.8 μm) at different detection wavelengths (from top to bottom 600, 700, 800, 900 nm) for e-beam excitation at the center of the disk. For quantitative signal strength reference, CL intensity is reported in "analog-to-digital converter units" (ADU), i.e., CCD camera counts, per steradian, and for the given 20 s acquisition time. We have no measured data for the 2.8 μm disk size at 900 nm. (b) 2D cross-cuts corresponding to patterns indicated by colored thick dotted boxes in (a).

wavenumbers due to ohmic losses, and for large $k'_{MIM}d$ concentration of radial LDOS structures at the disk edges.

Despite the qualitative similarities, there is no one-to-one quantitative correspondence between the measured and calculated spatial mode maps. We identify several probable reasons for this discrepancy. First, we have used patch antennas in the size range corresponding to strong angular directivity, i.e., disks several micrometers across. Such large disks have a dense plethora of modes, meaning that it is very difficult to obtain a one-to-one alignment of mode structure between experiment and theory. Second, we approximated the CL process in our model as entirely due to the LDOS of symmetric MIM resonances, since this is the mode that presents the largest Purcell factor in the gap for vertically oriented dipoles. This simplification neglects that the infinite layered system also supports an asymmetric MIM mode that can also contribute to CL, as analyzed by Cai et al. and Barnard et al.[34,35] Also, the ansatz of Filter et al.[23] ignores contributions at wave numbers different from k_{MIM} that could result from plasmons strongly localized at the patch edge. Especially at small patch size, neglecting such edge effects could deteriorate the comparison. Even if the simple model is accurate for LDOS (calculated with COMSOL), it need not be for CL, since in CL one needs to integrate contributions from along the electron beam path as worked out in the theory by García de Abajo and Kociak.[31] Fundamentally, it would be interesting to compare a full numerical evaluation of the theory by García de Abajo and Kociak[31] for CL with the full numerical evaluation of the Purcell factor that we report here, to assess why the Purcell factor does, but CL does not, trace the simple model by Filter et al.[23] Unfortunately, such a calculation appears prohibitively difficult, given that just mapping the Purcell factor in a single plane already requires on the order of several days of computation. In experiment, incoherent background radiation such as fluorescence emission of the silica layer can also contribute to the collected CL intensity. Incoherent background radiation should not be expected to give a featureless background. Rather, also fluorescence generated incoherently in the patch spacer can result in a spatially dependent and patch-size-dependent brightness, since the brightness of incoherent,

inefficient sources inside a photonic system will trace out its orientation-averaged radiative LDOS. Finally, inaccuracies in fabrication such as edge roughness evident in the SEM micrograph (Figure 1b) can influence the experimentally measured data.

ANGULAR EMISSION PATTERNS

Metal−insulator−metal patch antennas were first proposed for their large directivity. Fluorescence experiments have examined the directivity for single quantum dots for select quantum dot positions and disk sizes.[18] Cathodoluminescence provides a unique opportunity to map the directivity in a well-normalized fashion as a function of both disk size and where the system is excited. Moreover, the well-defined polarization and coherence of the induced transition dipole facilitate the interpretation and modeling of the radiation pattern, as will be discussed in this section.

Angular radiation patterns of the patch antennas are obtained by directly projecting the CL radiation collected by the parabolic mirror onto an imaging CCD where each pixel corresponds to a unique emission angle. A simple coordinate transformation[21] allows converting raw CCD images into polar (θ, φ) diagrams. Figure 6a shows the measured angular radiation patterns of patch antennas for different disk diameters and detection wavelengths, in each case with e-beam excitation at the disk center. Here, the disk diameter increases from left to right and the detection wavelength increases from top to bottom. Due to the symmetry of the structure and the excitation, radiation patterns are expected to be symmetric around the axis normal to the sample ($\theta = 0°$, center in each polar diagram). However, for some measurements, a slight asymmetry is seen. This asymmetry likely arises from our measurement strategy, since we collected radiation patterns in sequences where we use a finite sampling of e-beam positions (taking around 18 to 25 points) along the disk diameter. The sampling point targeted at the disk origin in some cases did not coincide exactly with the disk center, yielding a residual asymmetry. Overall, the radiation patterns show a strong dependence on the disk diameter and detection wavelength. Notably, the radiation patterns generally become more

directional with decreasing wavelength and increasing disk size, commensurate with the notion that the diffraction pattern of a coherently emitting disk of size d has a radiation pattern spread over an angle d/λ. The most directional radiation patterns show beam widths on the order of 30°. Moreover, the shorter-wavelength/larger-disk regime is accompanied by the emergence of sidelobes at larger angle. The appearance of more closely spaced fringes alongside main lobes is generally expected for larger antennas (smaller wavelength), on the basis of Fourier arguments: since the far field is approximately the Fourier transform of a near-field current distribution, more extended current distributions show sharper and denser diffraction rings. In addition, we note that a doughnut-like structure for the central lobe is evident for some data sets that are similar to the emission pattern of vertical dipoles at interfaces.

A clear correlation between the appearance of a doughnut-like pattern and the size of the disk or the detection wavelength is not immediately apparent in our experimental data. We note that a doughnut-like symmetry would be expected quite rigorously from symmetry in a fully coherent excitation experiment. Indeed, if one excites a cylindrically symmetric structure at its symmetry point with a z-oriented dipole, a decomposition of the emitted radiation into radial and azimuthal contributions must have zero azimuthal content. Any nonzero content would indicate a preferred handedness or a preferred in-plane linear polarization, which are both absent by symmetry. Since the emitted radiation must be radially polarized, one expects a null in the normal direction. Indeed, this notion is consistent with the null observed in previous CL experiments for transition radiation, excitation of small plasmon disks, and also the radiation patterns calculated in ref 18 for patch antennas. Radiation in the center of the polar images hence points to either symmetry-breaking in the excitation and light out-coupling of the structure or the presence of incoherent in-plane-polarized contributions to the CL signal, such as fluorescence generated in the silica spacer layer.

In an attempt to classify the reported radiation patterns and correlate the presence or absence of a central minimum to the degree to which an incoherent contribution is present in the sample, we have attempted to classify frequency/wavelength combinations as being on or off resonance according to the measured excitability maps. We expect those patterns measured on resonance to show a clear minimum at the normal radiation angle, as consistent with the coherent excitation and out-coupling of the MIM mode, while for patterns taken at an off-resonance combination we expect a stronger incoherent component. While not all 19 frequency/diameter combinations plotted in Figure 6 can be uniquely assigned as being exactly on or off resonance, we could assign four combinations as clearly on and seven as clearly off resonance. Indeed, according to the CL maps of Figure 5, we can identify $\lambda = 900$ nm at $d = 1.3$ μm and $d = 1.8$ μm, as well as the combinations $d = 0.6$ μm and $\lambda = 700$ nm and $d = 1.8$ μm and $\lambda = 600$ nm as combinations for which the CL maps clearly show a strong peak for excitations at the center of the disk. The corresponding radiation patterns of these four combinations are indicated by colored thick dotted squares surrounding the data in Figure 6a, and the corresponding 2D cross-cuts are plotted in Figure 6b. Notably for these combinations, radiation patterns indeed clearly present a doughnut-like symmetry. On the other hand, we identified combinations for which CL maps of Figure 5 show clear minima at the center of the disk. These "off-resonant" disk

combinations are indicated by thin black dotted lines in Figure 6a. In contrast to the "on-resonant" combinations, here the radiation patterns have peaks in the normal direction. Taking into account that for these combinations the mode feeding happens indirectly, this suggests that incoherent radiation processes are responsible for obscuring doughnut features from the radiation patterns. That the presence of the doughnut feature is sensitive to nonidealities in disk shape, disk–source alignment, or incoherent background contributions while still showing overall directivity is commensurate with the fluorescence measurements by Belacel et al.,[18] in which strong directivity but no central null in the radiation pattern of quantum dot clusters centered in the patch was found. In their work, they explained this by randomness in transition dipole orientation as well as positioning of the fluorophores.

As a measure of directivity of the patch antennas and in order to quantify the radiated beam width of the patch antenna, we extracted the half width at half-maximum (HWHM) values (ignoring the central null if present) from the 2D radiation patterns of Figure 6b and plotted sin(HWHM) as a function of the wavelength-normalized disk diameters (d/λ) in Figure 7.

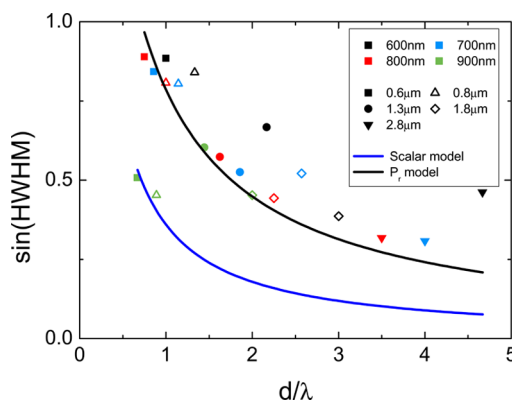**Figure 7.** Beam width of the patch antennas defined as sin(HWHM) as a function of wavelength-normalized disk diameters. Symbols: Measured beam width values. Lines: Calculated beam width using scalar model (blue) and radially polarized dipole model (black).

Here, measured values for different disk sizes are marked with different symbols and detection wavelengths are displayed by different colors. An overall decrease of the beam width is observed as the normalized disk size is increased, which is in agreement with the expectation on the basis of simple Fourier optics arguments, whereby the beam divergence of radiation scales inversely with source size.

We find that radiation patterns of patch antennas strongly depend on the position of the excitation source. In order to explore the position dependence of the radiation pattern, we measured the radiation pattern for e-beam excitations along cuts through the patch antennas from the left edge to the center to the right edge for all disk diameters and detection wavelengths. Figure 8a shows the radiation pattern of a typical patch antenna ($d = 2.8$ μm, $\lambda = 700$ nm) for different e-beam excitation positions from the left edge to the center of the disk. The emission angle of the main lobe clearly tilts away from the normal direction as the excitation position is shifted away from the disk center and varies from zenithal for central excitation to grazing, once the excitation reaches a point midway between center and edge excitation.
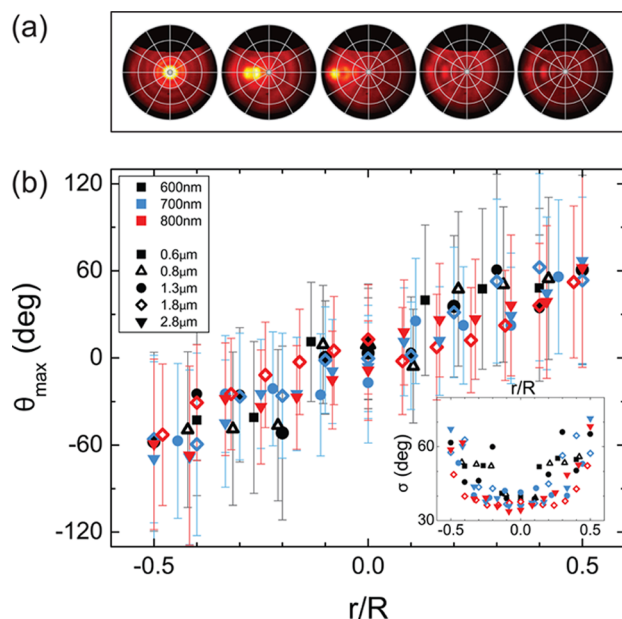
Figure 8. (a) Measured radiation pattern for different excitation positions for a typical patch antenna ($d = 2.8 \mu$m, $\lambda = 700$ nm). From left to right: e-beam excitation position at the center of the disk to the right edge of the disk. (b) Emission angle for a selected set of disk sizes and wavelengths as a function of normalized excitation distance from the disk center. Error bars indicate the angular width of the beam (standard deviation) with values plotted in the inset.

of the radiation pattern around the main lobe. The results are depicted as error bars in Figure 8b and are also plotted separately in the inset of Figure 8b. The directionality of the beam is highest for excitation of the disk at the center and decreases for excitations away from the disk center. A qualitative explanation is that the radiation is due to excitation of MIM plasmons as a cylindrical wave emanating from the excitation point that scatters out into the far field at the disk edge. For central excitation the entire edge of the disk radiates coherently with equal amplitude. As the excitation approaches the edge of the disk, however, only a fraction of the edge close to the excitation point dominates the radiated signal. Thus, shifting toward the edge reduces the effective source size and hence directionality.

■ SIMPLE MODEL FOR ANGULAR EMISSION PATTERNS

In order to analytically calculate radiation patterns of the patch antennas, we used a model based on the interference of the scattered fields at the edge of the disks. In this model, we assume that the local excitation at $\mathbf{r}_0$ launches a cylindrical outgoing wave

$$\frac{e^{ik_{\mathrm{MIM}}|\mathbf{r}-\mathbf{r}_0|}}{\sqrt{|\mathbf{r}-\mathbf{r}_0|}} \qquad (2)$$

In order to better illustrate the beam steering of the patch antennas, for a selected set of disk diameters and detection wavelengths, we examined 2D cross-cuts (not shown) generated by averaging the radiation pattern over 20 degree azimuthal range around $\phi = 90°$. We calculated the emission angle of the beam defined by the maximum lobe ($\theta_{\max}$) for disk sizes and wavelengths where beaming was pronounced at central excitation. We plot the results as a function of the excitation position r normalized to disk radius R in Figure 8b. The radiation angle depends linearly on the position of the e-beam excitation in a manner that is remarkably similar for all antenna and wavelength combinations. It should be noted that the plotted error bars do not indicate the error in determining $\theta_{\max}$ but serve to indicate the width of the beam in θ. For each excitation position, wavelength, and disk size, we extracted the angular width of the beam by calculating the standard deviation

in the patch that scatters out at the edge. In a simple analysis, the far-field radiation pattern is the Fourier transform of the amplitude and phase pattern imprinted on the disk edge. We will refer to this model as "scalar", as it does not contain polarization effects. In full-wave COMSOL simulations we have observed that if one sets up a MIM mode in the disk, the E-field at the disk edge is mainly polarized in the radial direction (three to one ratio relative to vertical polarization). A first estimate of the radiation pattern with polarization effects included is hence to discretize the disk edge as radially oriented dipoles with amplitude and phase given according to eq 2. Figure 9a shows a set of measured radiation patterns ($d = 1.3 \mu$m, $\lambda = 700$ nm), with Figure 9b and c showing the calculated radiation patterns for the radially polarized and scalar model. Reasonable correspondence is obtained in terms of the angle at which the central lobe occurs, its width, and the occurrence of side lobes at angles far from the main lobe. For comparison with experiment, calculated beam widths are plotted in Figure 7 for the scalar (blue line) and radially polarized dipole model (black line). A good agreement is observed with experiment for the
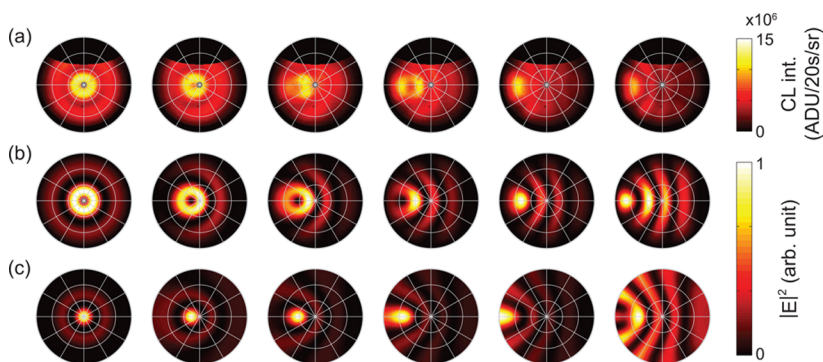

Figure 9. (a) Measured radiation pattern as a function of excitation position for a typical patch antenna ($d = 1.3 \mu$m, $\lambda = 700$ nm). Calculated radiation patterns from (b) radially polarized dipole model and (c) scalar model. From left to right: e-beam excitation position at the center of the disk to the right mid-edge ($x = r/2$) of the disk.

radial model, which is consistent with results from COMSOL simulations.

At first sight it might seem surprising that such excellent correspondence for radiation patterns is obtained taking as a model just the patch edge driven by the cylindrical outgoing wave of eq 2, without resorting at all to the complicated mode decomposition underlying the LDOS calculation. Explicit analysis shows that the mode decomposition, i.e., first projecting a local excitation at $\mathbf{r}_0$ into modes and then constructing radiation patterns by coherent superposition, likewise results in a good match to the observed radiation patterns. The physics resolving this seeming paradox is hidden in Figure 2b, which shows that especially large diameter disks support a large number of modes of various radial and azimuthal quantum numbers at any given frequency. The key physics is that the large number of modes supported by the disk is essentially a sufficiently complete set to build up the cylindrical wave assumed in eq 2, similar to the notion in standard optics that increasingly big objects have increasingly complex mode structures yet ultimately can be described increasingly well by simple ray optics arguments.

■ CONCLUSION

To conclude, we have reported a comprehensive study of plasmonic patch antennas in which we have shown a strong excitation position dependence of the angle-integrated cathodoluminescence, as well as the dependence of directivity on antenna size, wavelength, and driving position. As well, explained by an analytical model, patch antennas in the typical size regime for directional emission support a large number of overlapping modes of different angular and radial quantum numbers. For a dipole point source located in the MIM gap, the LDOS we find from full-wave simulations matches very well the analytical model based only on the symmetric MIM mode. We find that the CL maps, while qualitatively similar, quantitatively deviate, pointing to the fact that CL does not solely excite the MIM mode. Angular radiation patterns measured for central excitation and on a resonance present strongly directional doughnut beams, exactly as expected from symmetry and as was predicted but not observed in previous reports.[18] Moreover, our observations show that even incoherently and indirectly excited luminescence couples out in a directional fashion, without the beam pattern minimum exactly in the normal direction. Finally, the beam directivity and beam steering as a function of incident power is well explained without taking the mode structure into account at all, simply viewing the circular boundary as an outcoupler for the cylindrical MIM wave launched by the CL excitation.

■ METHODS

Disk Modes and LDOS. In order to calculate the eigenfrequencies of the patch antennas, we follow the separation of variables ansatz,[23] in which the eigenmodes can be written as

$$E_z^m(r, z) = a(z)J_m(k_{MIM}r)e^{im\phi} \tag{3}$$

Here $a(z)$ is the transverse mode profile obtained by solving for the infinitely extended MIM system, J_m is a Bessel function of the first kind, and $k_{MIM} = k_{MIM}{}' + ik_{MIM}{}''$ is the wavevector of the symmetric MIM mode, again found from the infinitely extended system. Next, to find a discrete set of eigenfrequencies, one needs to define a boundary condition. For instance,

requiring $E_z^m(r = \rho_{n,m}, Z) = 0$ as boundary condition would yield resonant disk radii $\rho_{n,m}$ as the roots of the Bessel function $k_{MIM}\rho_{n,m} = x_n(J_m)$. The mode numbers n and m correspond to radial and axial mode numbers, respectively. In fact, rather than taking as boundary condition $E_z^m(r = \rho_{n,m}, Z) = 0$, an accumulated phase ϕ_m upon reflection of the SPPs from the antenna edges can be translated into a correction in the resonant radii calculation as

$$2k_{MIM}'R + \varphi_m = 2x_n(J_m) \tag{4}$$

where $R = d/2$ is the physical radius of the disk. It has been shown that this formulation excellently describes the modes of simple metal disks, with a reflection phase ϕ that is disk size and frequency insensitive and can be calculated independently from simulation of reflection of the guided mode at a semi-infinite flat edge.[23]

For a given disk size, this procedure yields eigenfrequencies $\omega_{n,m}$ through inversion of the dispersion relation for all available mode numbers. Expanded in terms of eigenmodes, the local density of modes probed by a z-oriented dipole for a lossless system reads

$$N(\omega, r) \propto \sum_{n,m} |E_z^{n,m}(r)|^2 \delta(\omega^2 - \omega_{n,m}^2) \tag{5}$$

where the mode functions are understood to be normalized. In order to obtain a continuous LDOS spectrum, it is important to realize that each mode suffers a frequency broadening, which we assign according to the damping of the modes due to ohmic and radiation losses. In particular, we sum

$$N(\omega, r) \propto \sum_{n,m} |E_z^{n,m}(r)|^2 \mathcal{L}(\omega; \omega_{n,m}, \gamma) \tag{6}$$

where $\mathcal{L}(\omega; \omega_{n,m}, \gamma)$ denotes a Lorentzian (normalized to constant integral) centered at $\omega_{n,m}$ and with full width at half-maximum γ. It should be noted that in this procedure the only adjustable parameters are the reflection phase ϕ and the line width γ. The effect of changing the phase is to shift the entire structure of the resonance in frequency. For our calculations, the accumulated phase $\phi_m = -1.7$ and the empirical resonance line width[23] $\gamma/\omega = (2k_{MIM}''R)^2 + \gamma_0(1 + \omega_{norm}^b)^{-1}$ with $\gamma_0 = 0.1$, $b = 1.7$, and normalized frequency $\omega_{norm} = \omega/(1000 \text{ THz})$ are extracted from a COMSOL simulation (see below) by matching the resonance position and width of the fundamental mode.

COMSOL Simulation. In COMSOL we calculate the LDOS in the patch antenna by modeling a vertically oriented dipole source located in the silica spacer as a small (nanometer-long) current-carrying wire placed at mid-height in the gap. We record the power it emits into the environment that subsequently is dissipated in the metal, as well as the power it emits that is radiated into the far field. We have used the optical constants for gold of Johnson and Christy[25] as parametrized by Etchegoin[36] and performed a parametric sweep over 150 frequency points and 33 (31) dipole positions for a 0.6 μm (0.8 μm) disk size. The calculation time per point was approximately 2 min on a 2.0 GHz Intel Xeon E5-2620, where we have used mirror symmetry to reduce the computation volume to a half-space. Mapping Purcell factor versus frequency and radial position at just one height and dipole orientation thus takes over 6 days.

Sample Fabrication. Figure 1a schematically shows the geometrical structure of patch antennas used in our experiment.

The antennas are fabricated by first evaporating a 200 nm thick layer of gold on top of a glass substrate. This layer is optically thick. Next, a layer of positive-tone resist (ZEP520A) is spin-coated over the gold film, and circular patches are written in the resist using electron beam lithography. After developing the resist, circular disks are formed by evaporating a 50 nm thick layer of silica (SiO$_x$ where $x \approx 2$) followed by a 20 nm thick layer of gold at a rate of 0.5 nm/s and at an ambient pressure of 10^{-6} mbar. In order to enhance the adhesion of the gold layer to the silica, the sample is treated by an argon plasma before the gold layer is deposited. Finally, the resist is removed in a 65 °C hot bath of 1-methyl-2-pyrrolidinone (NMP) lift-off solvent. Before performing the measurements, the sample is cleaned with a mild O$_2$ plasma descum to remove any organic residues. Figure 1b shows a scanning electron micrograph of a fabricated patch antenna. Several patch antennas with disk diameters between 0.6 and 2.8 μm are fabricated on one sample.

Experimental Setup. In order to investigate the resonant modes of the patch antennas, we use ARCIS.[21,22] A 30 keV electron beam is scanned over a selected patch antenna in steps of 10 nm at a beam current of 0.8 nA. As reviewed by refs 34, 37, and 38, the high-energy electron beam as it approaches the metallic and dielectric interfaces of the antenna induces a vertical transient dipole moment, which locally excites the optical modes of the patch antenna. A part of the excited electric field may directly radiate into the far field, while another part funnels into the MIM mode and subsequently scatters out of the antenna edges into the far field. The overall radiated CL is then collected by a parabolic mirror that has a total collection angle of 1.46π sr. The light is guided to a spectrometer with a Si CCD detector or an imaging CCD detector for Fourier analysis, from which the angular radiation pattern can be obtained.[21]

■ AUTHOR INFORMATION

Corresponding Author
*E-mail: f.koenderink@amolf.nl.

■ REFERENCES

(1) Novotny, L.; van Hulst, N. F. Antennas for Light. *Nat. Photonics* **2011**, *5*, 83−90.
(2) Lee, K. G.; Chen, X. W.; Eghlidi, H.; Kukura, P.; Lettow, R.; Renn, A.; Sandoghdar, V.; Götzinger, S. A Planar Dielectric Antenna for Directional Single-Photon Emission and Near-Unity Collection Efficiency. *Nat. Photonics* **2011**, *5*, 166−169.
(3) *Optical Microcavities (Advanced Series in Applied Physics)*; Vahala, K., Eds.; World Scientific: Singapore, 2005; Vol. 5.
(4) Englund, D.; Fattal, D.; Waks, E.; Solomon, G.; Zhang, B.; Nakaoka, T.; Arakawa, Y.; Yamamoto, Y.; Vučković, J. Controlling the Spontaneous Emission Rate of Single Quantum Dots in a Two-Dimensional Photonic Crystal. *Phys. Rev. Lett.* **2005**, *95*, 013904.
(5) Noda, S.; Fujita, M.; Asano, T. Spontaneous-Emission Control by Photonic Crystals and Nanocavities. *Nat. Photonics* **2007**, *1*, 449−458.
(6) Curto, A. G.; Volpe, G.; Taminiau, T. H.; Kreuzer, M. P.; Quidant, R.; van Hulst, N. F. Unidirectional Emission of a Quantum Dot Coupled to a Nanoantenna. *Science* **2010**, *329*, 930−933.
(7) de Waele, R.; Koenderink, A. F.; Polman, A. Tunable Nanoscale Localization of Energy on Plasmon Particle Arrays. *Nano Lett.* **2007**, *7*, 2004−2008.
(8) Koenderink, A. F. Plasmon Nanoparticle Array Waveguides for Single Photon and Single Plasmon Sources. *Nano Lett.* **2009**, *9*, 4228−4233.
(9) Kosako, T.; Kadoya, Y.; Hofmann, H. F. Directional Control of Light by a Nano-Optical Yagi-Uda Antenna. *Nat. Photonics* **2010**, *4*, 312−315.
(10) Bernal Arango, F.; Kwadrin, A.; Koenderink, A. F. Plasmonic Antennas Hybridized with Dielectric Waveguides. *ACS Nano* **2012**, *6*, 10156−10167.
(11) Aouani, H.; Mahboub, O.; Devaux, E.; Rigneault, H.; Ebbesen, T. W.; Wenger, J. Plasmonic Antennas for Directional Sorting of Fluorescence Emission. *Nano Lett.* **2011**, *11*, 2400−2406.
(12) Yi, J. M.; Cuche, A.; Devaux, E.; Genet, C.; Ebbesen, T. W. Beaming Visible Light with a Plasmonic Aperture Antenna. *ACS Photonics* **2014**, *1*, 365−370.
(13) Langguth, L.; Punj, D.; Wenger, J.; Koenderink, A. F. Plasmonic Band Structure Controls Single-Molecule Fluorescence. *ACS Nano* **2013**, *7*, 8840−8848.
(14) Rodriguez, S. R. K.; Lozano, G.; Verschuuren, M. A.; Gomes, R.; Lambert, K.; De Geyter, B.; Hassinen, A.; Van Thourhout, D.; Hens, Z.; Gómez Rivas, J. Quantum Rod Emission Coupled to Plasmonic Lattice Resonances: A Collective Directional Source of Polarized Light. *Appl. Phys. Lett.* **2012**, *100*, 111103.
(15) Rolly, B.; Stout, B.; Bonod, N. Boosting the Directivity of Optical Antennas with Magnetic and Electric Dipolar Resonant Particles. *Opt. Express* **2012**, *20*, 20376.
(16) Coenen, T.; Bernal Arango, F.; Koenderink, A. F.; Polman, A. Directional Emission from a Single Plasmonic Scatterer. *Nat. Commun.* **2014**, *5*, 3250.
(17) Esteban, R.; Teperik, T. V.; Greffet, J. J. Optical Patch Antennas for Single Photon Emission Using Surface Plasmon Resonances. *Phys. Rev. Lett.* **2010**, *104*, 026802.
(18) Belacel, C.; Habert, B.; Bigourdan, F.; Marquier, F.; Hugonin, J. P.; Michaelis de Vasconcellos, S.; Lafosse, X.; Coolen, L.; Schwob, C.; Javaux, C.; Dubertret, B.; Greffet, J. J.; Senellart, P.; Maitre, A. Controlling Spontaneous Emission with Plasmonic Optical Patch Antennas. *Nano Lett.* **2013**, *13*, 1516−1521.
(19) Schoen, D. T.; Coenen, T.; García de Abajo, F. J.; Brongersma, M. L.; Polman, A. The Planar Parabolic Optical Antenna. *Nano Lett.* **2013**, *13*, 188−193.
(20) Balanis, C. A. *Antenna Theory: Analysis and Design*, 3rd ed.; Wiley Interscience; Hoboken, NJ, 2005; Chapter 14.
(21) Coenen, T.; Vesseur, E. J. R.; Polman, A. Angle-Resolved Cathodoluminescence Spectroscopy. *Appl. Phys. Lett.* **2011**, *99*, 143103.
(22) Sapienza, R.; Coenen, T.; Renger, J.; Kuttge, M.; van Hulst, N. F.; Polman, A. Deep-Subwavelength Imaging of the Modal Dispersion of Light. *Nat. Mater.* **2012**, *11*, 781−787.
(23) Filter, R.; Qi, J.; Rockstuhl, C.; Lederer, F. Circular Optical Nanoantennas: An Analytical Theory. *Phys. Rev. B* **2012**, *85*, 125429.
(24) Minkowski, F.; Wang, F.; Chakrabarty, A.; Wei, Q. H. Resonant Cavity Modes of Circular Plasmonic Patch Nanoantennas. *Appl. Phys. Lett.* **2014**, *104*, 021111.
(25) Johnson, P. B.; Christy, R. W. Optical Constants of the Noble Metals. *Phys. Rev. B* **1972**, *6*, 4370−4379.

(26) Dionne, J. A.; Verhagen, E.; Polman, A.; Atwater, H. A. Are Negative Index Materials Achievable with Surface Plasmon Waveguides? A Case Study of Three Plasmonic Geometries. *Opt. Express* **2008**, *16*, 19001−19017.

(27) Miyazaki, H. T.; Kurokawa, Y. Squeezing Visible Light Waves into a 3-nm-Thick and 55-nm-Long Plasmon Cavity. *Phys. Rev. Lett.* **2006**, *96*, 097401.

(28) Miyazaki, H. T.; Kurokawa, Y. Controlled Plasmon Resonance in Closed Metal/Insulator/Metal Nanocavities. *Appl. Phys. Lett.* **2006**, *89*, 211126.

(29) Kuttge, M.; Cai, W.; García de Abajo, F. J.; Polman, A. Dispersion of Metal-Insulator-Metal Plasmon Polaritons Probed by Cathodoluminescence Imaging Spectroscopy. *Phys. Rev. B* **2009**, *80*, 033409.

(30) Kuttge, M.; García de Abajo, F. J.; Polman, A. Ultrasmall Mode Volume Plasmonic Nanodisk Resonators. *Nano Lett.* **2010**, *10*, 1537−1541.

(31) García de Abajo, F. J.; Kociak, M. Probing the Photonic Local Density of States with Electron Energy Loss Spectroscopy. *Phys. Rev. Lett.* **2008**, *100*, 106804.

(32) Harrison, W. A. *Solid State Theory*; Dover Publications: New York, 1979.

(33) Coenen, T.; Vesseur, E. J. R.; Polman, A. Deep Subwavelength Spatial Characterization of Angular Emission from Single-Crystal Au Plasmonic Ridge Nanoantennas. *ACS Nano* **2012**, *6*, 1742−1750.

(34) Cai, W.; Sainidou, R.; Xu, J.; Polman, A.; García de Abajo, F. J. Efficient Generation of Propagating Plasmons by Electron Beams. *Nano Lett.* **2009**, *9*, 1176−1181.

(35) Barnard, E. S.; Coenen, T.; Vesseur, E. J. R.; Polman, A.; Brongersma, M. L. Imaging the Hidden Modes of Ultrathin Plasmonic Strip Antennas by Cathodoluminescence. *Nano Lett.* **2011**, *11*, 4265−4269.

(36) Etchegoin, P. G.; Le Ru, E. C.; Meyer, M. An Analytic Model for the Optical Properties of Gold. *J. Chem. Phys.* **2006**, *125*, 164705.

(37) García de Abajo, F. J. Optical Excitations in Electron Microscopy. *Rev. Mod. Phys.* **2010**, *82*, 209.

(38) van Wijngaarden, J. T.; Verhagen, E.; Polman, A.; Ross, C. E.; Lezec, H. J.; Atwater, H. A. Direct Imaging of Propagation and Damping of Near-Resonance Surface Plasmon Polaritons using Cathodoluminescence Spectroscopy. *Appl. Phys. Lett.* **2006**, *88*, 221111.